

# UPCommons

## Portal del coneixement obert de la UPC

<http://upcommons.upc.edu/e-prints>

---

Aquesta és una còpia de la versió *author's final draft* d'un article publicat a la revista *Journal of Fluids and Structures*.

URL d'aquest document a UPCommons E-prints:

<http://hdl.handle.net/2117/133394>

---

### Article publicat / Published paper:

Naseri, A. [et al.]. A second-order time accurate semi-implicit method for fluid–structure interaction problems. (2019) *Journal of fluids and structures*, vol. 86, p. 135-155. DOI: <[10.1016/j.jfluidstructs.2019.02.007](https://doi.org/10.1016/j.jfluidstructs.2019.02.007)>.

© <2019>. Aquesta versió està disponible sota la llicència CC-BY- NC-ND 4.0 <http://creativecommons.org/licenses/by-nc-nd/4.0/>

# A Second-Order Time Accurate Semi-Implicit Method for Fluid-Structure Interaction Problems

Alireza Naseri, Ignacio Gonzalez, Ahmad Amani, Carlos David  
Pérez-Segarra\*, Assensi Oliva

*Heat and Mass Transfer Technological Center (CTTC),  
Universitat Politècnica de Catalunya-BarcelonaTech (UPC),  
ESEIAAT, Colom 11, 08222 Terrassa (Barcelona), Spain*

---

## Abstract

This paper is concerned with numerical solution of fluid-structure interaction (FSI) problems involving an incompressible viscous flow and an elastic structure. A semi-implicit partitioned method with second-order temporal accuracy is proposed. The method separates the pressure term of the fluid equations and strongly couples it to the structure, while the remaining fluid terms and the geometrical nonlinearities are treated explicitly. A second-order projection method is used to solve the fluid equations and also as a framework for the FSI coupling. Particular attention is paid to the boundary conditions for fluid equations and the accuracy of the fluid pressure on the common interface. The proposed coupling method retains the second-order accuracy for fully-coupled nonlinear FSI problems. Extensive numerical tests are carried out on a number of benchmark FSI problems and the second-order temporal accuracy for all the variables of interest (fluid velocity and pressure, and structural displacement) is demonstrated.

*Keywords:* Fluid-Structure Interaction, Partitioned Method, Semi-Implicit Coupling, Projection Method, Second-Order Temporal Accuracy

---

---

\*Corresponding author.

*Email address:* `cttc@cttc.upc.edu` (Carlos David Pérez-Segarra)

## 1. INTRODUCTION

Fluid-structure interaction (FSI) refers to problems with bilateral interaction between a fluid flow and a moving or deforming structure. Fluid flow exerts surface forces on the structure which causes its deformation. The movement of the solid boundary, in return, alters the flow field. A very wide range of applications is cited for FSI, from study of blood flow inside the cardiovascular system (e.g. [1, 2]), to the study of vortex-induced vibration of submerged structures in offshore engineering (e.g. [3, 4]).

A popular class of numerical methods to solve FSI problems is called partitioned methods. These methods use separate solvers for fluid and structural sub-problems and adopt a coupling technique to account for the interaction of the domains. One of the strong advantages of the partitioned methods is the possibility to use the most adapted and well-validated numerical methods for each sub-problem. Moreover, it allows using previously developed and optimized fluid and structural solver codes [5, 6]. Partitioned methods are generally divided into explicit (or loosely coupled) and implicit (or strongly coupled) techniques. Explicit partitioned methods solve the fluid and structural equations in sequence and only once per time step. These methods do not satisfy the exact equilibrium conditions on the interface, which causes instability issues in a range of FSI problems (the so-called added-mass instability) [7, 8]. Implicit methods, on the other hand, use coupling iterations between fluid and structural solvers to enforce the equilibrium condition on the interface. These methods are stable for problems with strong added-mass effect, however, their computational cost is generally high due to the repetitive solution of the governing equations at each time step [5, 6].

In a partitioned method, the equilibrium conditions on the interface are applied as boundary conditions on each sub-problem, through a decomposition method. Dirichlet-Neumann decomposition is a classical and widely used method in partitioned solution of FSI problems (see e.g. [9, 10, 11]). The name of the method indicates that a Dirichlet boundary condition is used for the fluid equations and a Neumann boundary condition for the structure. Therefore, the fluid equations are solved for a known displacement of the solid, while the structural equations are solved for a known stress on the interface. This is a simple decomposition and it is consistent with the most common numerical methods for fluid and structural equations. There is a more recent class of Robin-based decomposition methods that use a Robin boundary condition for the fluid and either a Robin or Neumann boundary

condition for the structure [12, 13, 14]. Robin-based methods are gaining popularity as they allow a loosely-coupled and yet added-mass-free FSI coupling. However, they require using an especial fluid solver capable of handling a Robin boundary condition. Thus they might not be readily usable with some of the most common fluid solvers. In this work we use a Dirichlet-Neumann decomposition for its advantages of simplicity and consistency.

Instability in loosely coupled methods with Dirichlet-Neumann decomposition is caused by the added-mass effect. The added-mass instability is, in principle, independent of the time step size or the particular discretization method used for each sub-problem solver. It is rather inherent to the coupling method and it has a particularly strong effect in FSI problems with incompressible flow and similar densities of fluid and solid [7, 8]. It is argued that the fluid pressure term is the main contributor to the added-mass effect and its explicit coupling would cause instability issues [7]. This was the main motivation for a new category of partitioned methods, first proposed by Fernandez et al. [15], and called semi-implicit methods. In a semi-implicit coupling method, the fluid pressure term is segregated and strongly coupled to the structure, while the remaining fluid terms are only loosely coupled. Segregation of the pressure term could be naturally achieved by using a classical Chorin-Temam projection method [16]. Strong coupling of the fluid pressure and structural deformation eliminates the added-mass instability issue, while loose coupling of the remaining fluid terms helps avoiding excessive computational cost [15].

A similar semi-implicit method was proposed by Breuer et al. [17] where the geometrical nonlinearities are also coupled implicitly. Astorino et al. [18] improved the stability of the method in [15] by using a specific Robin treatment of the explicit part of the coupling derived from Nitsche’s method. An enhanced semi-implicit method was proposed by Naseri et al. [19, 20]. Numerical tests showed that the accuracy of the method in a practical problem is very similar to a fully implicit partitioned method, while its computational cost is remarkably smaller [20]. The application of the method was extended to turbulent flow [21, 22] and non-Newtonian fluids [23]. Other similar semi-implicit methods are presented in [24, 25] which use a characteristic-based split (CBS) scheme instead of Chorin-Temam projection method. It should be noted that these semi-implicit methods are different from the methods in [26, 27, 28]—which are also sometimes called semi-implicit. In the methods in [26, 27, 28], the location of the interface is treated explicitly (extrapolated in time) and the fluid mesh is moved once in a time step, however, the fluid

and structural equations are solved completely at each coupling iteration (i.e. only the geometrical nonlinearities are treated explicitly).

Semi-implicit coupling techniques rely on a projection method to solve the fluid equations and segregate the pressure term. The fluid pressure term is then strongly coupled to the structure via coupling iterations. Thus, the projection method does not only serve to solve the fluid equations but also as a framework for the FSI coupling. The semi-implicit methods in [15, 18, 20] have used a first-order Chorin-Temam projection method, while [24] have used a first-order CBS scheme for this purpose. Therefore, the overall temporal accuracy of these methods is at most one. Methods in [17, 25] have used apparently second-order pressure splitting schemes, but no error analysis (neither analytical nor numerical) was presented to show that a second-order temporal accuracy was actually achieved for a FSI solution. Extending temporal accuracy of projection methods to higher orders is not straightforward, as discussed in [29, 30, 31]. Although it is relatively easy to achieve second-order accuracy for velocity, fluid pressure remains only first-order accurate for many projection methods in the literature [29, 30, 31]. Considering that the fluid pressure is a main acting force on the structure, second-order accuracy for pressure is essential to achieve a second-order FSI solution. Moreover, mesh-conforming FSI solution methods require solving the Arbitrary Lagrangian–Eulerian (ALE) form of the Navier-Stokes equations on a moving mesh. A method for solving the fluid equations on a dynamic grid and evaluating the geometrical terms arising from the ALE formulation does not necessarily preserve the order of accuracy of the method on a fixed grid (see e.g. [32]). Furthermore, if the FSI coupling technique is not properly designed, the second-order accuracy for the coupled problem is not guaranteed, even though each sub-problem possessed such accuracy.

In point of fact, there are few second-order time accurate methods among other types of implicit and explicit partitioned methods in the literature. Farhat et al. [33] proposed a second-order loosely coupled partitioned method for FSI problems in aeroelasticity. This method is explicit so it is not suitable for strong added-mass problems. Nobile et al. [27] reported up to fourth-order time-accurate implicit partitioned methods. In some versions of the proposed method, the location of the interface is extrapolated in time (explicit treatment of geometrical nonlinearities). Liu et al. [28] proposed a second-order technique based on a combined field method with explicit treatment of the interface location. The method was shown to be stable regardless of the mass ratio. Oyekole et al. [34] proposed a second order partitioned method based

on a Robin boundary condition for the fluid. The structural inertia term is included in the Robin boundary condition for the fluid which makes the scheme stable for strong added-mass cases.

In this work, we propose a semi-implicit partitioned FSI method that is second-order accurate in time. This is, to the best of our knowledge, the first semi-implicit partitioned FSI method with a demonstrated second-order accuracy. A projection method is used to segregate the fluid pressure term, which is then strongly coupled to the structure via coupling iterations. In order to obtain second-order accuracy in a FSI solution, four important steps are taken:

- i) Presenting an incremental projection method and discretization in time that actually yields second-order accuracy for fluid pressure, as well as velocity.
- ii) Deriving specific projection-consistent boundary conditions for all fluid boundaries including the interface with the solid.
- iii) Developing an ALE scheme on a moving grid and evaluating the arisen geometrical terms with second-order accuracy.
- iv) Properly coupling the fluid and structural solvers in order to retain the second-order accuracy for a coupled nonlinear FSI problem.

The second-order accuracy of the method for realistic nonlinear FSI problems is demonstrated through rigorous numerical tests. Three widely distinct FSI test cases are studied and an analysis is made to show the second-order rate of convergence of the error.

The remaining of this paper is organized as follows. In section 2 the governing equations for each sub-problem and the coupling conditions are presented. Section 3 describes the proposed numerical method, while numerical tests are presented in section 4. Section 5 summarizes and concludes the article.

## 2. GOVERNING EQUATIONS

In this section, the governing equations for each sub-problem domain and the coupling conditions on the interface are presented. The fluid and structural domains are referred to as  $\Omega_f(t) \subset \mathbb{R}^3 \times (0, T)$  and  $\Omega_s(t) \subset \mathbb{R}^3 \times (0, T)$  respectively, as they both vary in time  $t \in (0, T)$ . The fluid-structure interface is the shared boundary of the domains, denoted by  $\Gamma(t) = \partial\Omega_f(t) \cap \partial\Omega_s(t)$ .

### 2.1. Fluid equations

The unsteady flow of an incompressible viscous fluid is governed by the Navier-Stokes equations. An Arbitrary Lagrangian-Eulerian (ALE) formulation of these equations in a moving domain is given by:

$$\frac{\partial \mathbf{u}}{\partial t} + \mathbf{c} \cdot \nabla \mathbf{u} = \frac{1}{\rho_f} \nabla \cdot \boldsymbol{\sigma}_f \quad (1)$$

$$\nabla \cdot \mathbf{u} = 0 \quad (2)$$

where  $\mathbf{u}$  is the fluid velocity and  $\rho_f$  the fluid density. Vector  $\mathbf{c}$  is the ALE convective velocity  $\mathbf{c} = \mathbf{u} - \mathbf{w}$ , which is the fluid velocity relative to a domain moving with a velocity  $\mathbf{w}$ . The stress tensor  $\boldsymbol{\sigma}_f$  is defined for a Newtonian fluid as:

$$\boldsymbol{\sigma}_f = -p\mathbf{I} + 2\mu_f\boldsymbol{\gamma} \quad (3)$$

where  $p$  is the fluid pressure,  $\mathbf{I}$  the unit tensor,  $\mu_f$  the dynamic viscosity of the fluid and  $\boldsymbol{\gamma}$  the strain rate tensor given by:

$$\boldsymbol{\gamma} = \frac{1}{2}(\nabla \mathbf{u} + \nabla \mathbf{u}^T) \quad (4)$$

### 2.2. Structural equations

The structural domain is governed by the nonlinear elastodynamics equation:

$$\rho_s \frac{\partial^2 \mathbf{d}}{\partial t^2} = \nabla \cdot \mathbf{P} \quad (5)$$

where  $\mathbf{d}$  stands for the structural position with respect to the reference configuration, and the structural density is shown by  $\rho_s$ . The tensor  $\mathbf{P}$  is the first Piola-Kirchhoff tensor, which is related to the Cauchy stress tensor  $\boldsymbol{\sigma}_s$  by:

$$\mathbf{P} = J\boldsymbol{\sigma}_s\mathbf{F}^{-T} \quad (6)$$

where  $\mathbf{F}$  is the deformation gradient  $\mathbf{F} = \nabla \mathbf{d}$  and  $J$  its determinant ( $J = \det(\mathbf{F})$ ).

The FSI method is presented for a general structure, however, for the numerical tests, different simplified structural models are considered which are described for each test case in section 4.

### 2.3. Coupling conditions

The coupling conditions apply at the interface  $\Gamma$  and account for the interaction of the domains. They are derived from the kinematic and dynamic equilibrium between the domains, which yield to the following conditions on a non-slip type interface:

$$\mathbf{u}_\Gamma = \frac{\partial \mathbf{d}_\Gamma}{\partial t} \quad (7)$$

$$\boldsymbol{\sigma}_s \mathbf{n}_\Gamma = \boldsymbol{\sigma}_f \mathbf{n}_\Gamma \quad (8)$$

for any  $\mathbf{x} \in \Gamma$ , where  $\mathbf{n}_\Gamma$  is the unit normal vector on the interface. Equation (7) represents the equality of the velocities of the fluid and the structure on the interface to assure the kinematic equilibrium. Equation (8) represents the equality of the traction on the interface for dynamic equilibrium.

## 3. NUMERICAL METHOD

In this section, the temporal discretization of the governing equations and the FSI coupling method are presented. This time-discretized set of equations are independent of the choice for spatial discretization, which could be carried out using either a finite-volume or a finite-element method. The spatial discretization methods used for the numerical tests are described in Appendix 1.

### 3.1. Fluid solver

Using a second-order central scheme around the mid-time-step point  $t^{n+1/2}$  for the transient term of the momentum equation, a second-order time-discretized form of the Eq. (1) and (2) reads:

$$\frac{\mathbf{u}^{n+1} - \mathbf{u}^n}{\Delta t} = -(\mathbf{c} \cdot \nabla \mathbf{u})^{n+1/2} + \frac{\mu_f}{\rho_f} \nabla^2 \mathbf{u}^{n+1/2} - \frac{1}{\rho_f} \nabla p^{n+1/2} \quad (9)$$

$$\nabla \cdot \mathbf{u}^{n+1} = 0 \quad (10)$$

for any  $\mathbf{x} \in \Omega_f^{n+1}$ , and a proper set of boundary conditions:

$$\left\{ \begin{array}{ll} \mathbf{u}_\Gamma^{n+1} = \frac{\partial \mathbf{d}_\Gamma^{n+1}}{\partial t} & \text{on } \Gamma^{n+1} \\ \mathbf{u}_{\partial_D}^{n+1} = \mathbf{u}_b & \text{on } \partial_D \Omega_f^{n+1} \\ \frac{\partial \mathbf{u}^{n+1}}{\partial \mathbf{n}}|_{\partial_N} = 0 & \text{on } \partial_N \Omega_f^{n+1} \end{array} \right. \quad (11)$$

where  $\partial_D$  and  $\partial_N$  represent, respectively, the Dirichlet and Neumann fluid boundaries,  $\mathbf{n}$  is the normal unit vector and  $\mathbf{u}_b$  is the assigned velocity on the boundary. The boundary condition on the fluid-structure interface  $\Gamma^{n+1}$  comes from the kinematic equilibrium condition and is applied as a Dirichlet boundary condition for the fluid equations (Eq. (11)<sub>1</sub>).

We use an incremental pressure-correction projection method, similar to [35, 36], to solve the momentum equation. Thus, an intermediate velocity is evaluated using the last known pressure field. Unlike the original projection method of Chorin-Temam [16], this method does not impose a formal first-order splitting error. We use an explicit Adams-Bashforth method for the convective term and a Crank-Nicolson method for the diffusive term. Therefore, the intermediate velocity field,  $\mathbf{u}^*$ , is evaluated as:

$$\frac{\mathbf{u}^* - \mathbf{u}^n}{\Delta t} = -\left[\frac{3}{2}(\mathbf{c} \cdot \nabla \mathbf{u})^n - \frac{1}{2}(\mathbf{c} \cdot \nabla \mathbf{u})^{n-1}\right] + \frac{\mu_f}{2\rho_f}(\nabla^2 \mathbf{u}^* + \nabla^2 \mathbf{u}^n) - \frac{1}{\rho_f} \nabla p^{n-1/2} \quad (12)$$

This velocity field is then projected onto a space of divergence-free vector fields:

$$\mathbf{u}^* = \mathbf{u}^{n+1} + \frac{\Delta t}{\rho_f} \nabla \phi^{n+1} \quad (13)$$

$$\nabla \cdot \mathbf{u}^{n+1} = 0 \quad (14)$$

where  $\phi^{n+1}$  is a scalar field obtained by:

$$\nabla^2 \phi^{n+1} = \frac{\rho_f}{\Delta t} \nabla \cdot \mathbf{u}^* \quad (15)$$

Substituting Eq. (13) into Eq. (12) and comparing it to Eq. (9), the equation to recover the fluid pressure at the mid-time step is obtained as:

$$p^{n+1/2} = p^{n-1/2} + \phi^{n+1} - \frac{\mu_f \Delta t}{2\rho_f} \nabla^2 \phi^{n+1} \quad (16)$$

Pressure at the new time station  $t^{n+1}$  could be evaluated by a second-order extrapolation from half-time levels:

$$p^{n+1} = \frac{3}{2}p^{n+1/2} - \frac{1}{2}p^{n-1/2} \quad (17)$$

Pressure at  $t^{n+1}$  is not used in the discretized fluid equations but it is needed to evaluate the fluid force on the structure at the new time step.

**Remark 1.** The last term in the pressure recovery equation (Eq. (16)) was missed in some projection methods, however, it is essential for retaining the second-order accuracy for pressure up to the boundary. It was first introduced (in a slightly different form) in [37]. A common practice in the literature is to use a uniform Neumann boundary condition (zero normal gradient) for the Poisson's equation for  $\phi$  (Eq. (15)). Without the last term of Eq. (16), the Neumann boundary condition for the scalar field  $\phi$  transmits to the pressure itself and creates an artificial boundary layer which degrades the accuracy. Interested readers are advised to consult [29, 31] for some analyses. The boundary conditions in the present work are further discussed in the next section.

**Remark 2.** A common inaccuracy in many methods in the literature is omitting the extrapolation of pressure (Eq. (17)) and evaluating  $p^{n+1}$  by Eq. (16). However, that would not be consistent with the central time discretization at Eq. (9). If the pressure at Eq. (16) were considered to be at time  $t^{n+1}$  instead of  $t^{n+1/2}$ , it will always carry a first-order error due to the time lag.

### 3.2. Boundary conditions

In this section the boundary conditions for the predicted velocity  $\mathbf{u}^*$  and the scalar field  $\phi$  are described in detail. We recognize three regions of the boundary with different boundary conditions, as in Eq. (11). The first region is the fluid-structure interface  $\Gamma$ . The boundary condition for velocity comes from the kinematic equilibrium on the interface (Eq. (11)<sub>1</sub>). Using a second-order backward difference scheme it reads:

$$\mathbf{u}_\Gamma^{n+1} = \frac{\partial \mathbf{d}_\Gamma^{n+1}}{\partial t} = \frac{3\mathbf{d}_\Gamma^{n+1} - 4\mathbf{d}_\Gamma^n + \mathbf{d}_\Gamma^{n-1}}{2\Delta t} \quad \text{on } \Gamma^{n+1} \quad (18)$$

which is a Dirichlet boundary condition for velocity. However, there is no specific boundary condition for pressure. A common approach is to use a uniform Neumann boundary condition (zero normal gradient on the boundary) for pressure. Such a boundary condition would create an artificial boundary layer near the interface that would degrade the accuracy. Numerical tests in [29, 31] demonstrate the artificial boundary layer and the loss of accuracy on a wall boundary.

In this work we use a zero normal gradient boundary condition for the scalar field  $\phi$ :

$$\mathbf{n} \cdot \nabla \phi^{n+1}|_{\Gamma} = 0 \quad \text{on } \Gamma^{n+1} \quad (19)$$

which is a very convenient boundary condition for the Poisson equation (Eq. (15)). However, because of the last term in the pressure recovery equation, Eq. (16), the Neumann boundary condition is not transmitted to the pressure itself and the artificial boundary layer is avoided. This is essential to achieve a second-order accuracy for pressure up to the boundary.

For the predicted velocity field, we derive a boundary condition consistent with Eq. (13):

$$\mathbf{u}_{\Gamma}^* = \mathbf{u}_{\Gamma}^{n+1} + \frac{\Delta t}{\rho_f} \nabla \phi^{n+1}|_{\Gamma} \quad (20)$$

Dividing Eq. (20) into its components using the normal and tangential unit vectors on the boundary,  $\mathbf{n}$  and  $\boldsymbol{\tau}$ , we get:

$$\mathbf{n} \cdot \mathbf{u}^*|_{\Gamma} = \mathbf{n} \cdot \mathbf{u}^{n+1}|_{\Gamma} + \frac{\Delta t}{\rho_f} \mathbf{n} \cdot \nabla \phi^{n+1}|_{\Gamma} \quad (21)$$

$$\boldsymbol{\tau} \cdot \mathbf{u}^*|_{\Gamma} = \boldsymbol{\tau} \cdot \mathbf{u}^{n+1}|_{\Gamma} + \frac{\Delta t}{\rho_f} \boldsymbol{\tau} \cdot \nabla \phi^{n+1}|_{\Gamma} \quad (22)$$

Considering boundary conditions (18) and (19), and using an explicit extrapolation for the gradient term, the boundary conditions for predicted velocity are obtained as:

$$\begin{cases} \mathbf{n} \cdot \mathbf{u}^*|_{\Gamma} = \mathbf{n} \cdot \frac{\partial \mathbf{d}_{\Gamma}^{n+1}}{\partial t}|_{\Gamma} \\ \boldsymbol{\tau} \cdot \mathbf{u}^*|_{\Gamma} = \boldsymbol{\tau} \cdot \frac{\partial \mathbf{d}_{\Gamma}^{n+1}}{\partial t}|_{\Gamma} + \frac{\Delta t}{\rho_f} \boldsymbol{\tau} \cdot (2\nabla \phi^n - \nabla \phi^{n-1})|_{\Gamma} \end{cases} \quad \text{on } \Gamma^{n+1} \quad (23)$$

Similar boundary conditions are used for other fluid boundary regions with a Dirichlet boundary condition for velocity ( $\partial_D \Omega_f^{n+1}$  in Eq. (11)), including stationary walls and flow inlets with a known velocity. Equations (23) are modified to use the assigned velocity in place of the interface velocity (e.g.  $\mathbf{u}_b = 0$  for stationary walls).

The third fluid boundary region is where a Neumann boundary condition is used for velocity (referred to as  $\partial_N \Omega_f^{n+1}$  in Eq. (11)). Pressure on the boundary could be specified by a Dirichlet boundary condition (e.g. an outlet with a known discharge pressure) or left without any specific boundary condition (e.g. in openings and vents with unknown pressure). In case of a Dirichlet boundary condition for pressure, an equivalent Dirichlet condition is applied on the scalar field  $\phi$ . In the case that no physical boundary condition is specified for pressure, a zero normal gradient boundary condition is used for  $\phi$ . Therefore, the set of boundary conditions are as follows:

$$\left\{ \begin{array}{l} \frac{\partial \mathbf{u}^{n+1}}{\partial \mathbf{n}} \Big|_{\partial_N} = 0 \\ \phi^{n+1} = \phi_b \quad \text{or} \quad \mathbf{n} \cdot \nabla \phi^{n+1} \Big|_{\partial_N} = 0 \end{array} \right. \quad \text{on } \partial_N \Omega_f^{n+1} \quad (24)$$

Again a consistent boundary condition for the predicted velocity is derived. Getting normal derivative of Eq. (13) and applying condition (24)<sub>1</sub>, it reads:

$$\frac{\partial \mathbf{u}^*}{\partial \mathbf{n}} \Big|_{\partial_N} = \frac{\Delta t}{\rho_f} \frac{\partial}{\partial \mathbf{n}} \nabla \phi^{n+1} \Big|_{\partial_N} \quad \text{on } \partial_N \Omega_f^{n+1} \quad (25)$$

Depending on the type of boundary condition for  $\phi$  (conditions (24)<sub>2</sub>), the normal or tangential component of the right hand side term in Eq. (25) might be zero. The non-zero components of the derivative of the gradient are evaluated on the boundary and the consistent boundary condition (Eq. (25)) is applied on the predicted velocity field.

**Remark 3.** It should be mentioned that similar consistent boundary conditions for simpler boundary of an stationary wall (Dirichlet boundary condition for velocity) were proposed in [38, 29].

### 3.3. Dynamic mesh

We use a conforming mesh technique, which means the fluid mesh moves to adapt to the new location of the interface. A parallel moving mesh technique, based on radial basis function interpolation method [39], is used to move the fluid grid in accordance to the new location of the interface and define the discretized fluid domain at the new time step  $\Omega_f^{n+1}$ .

The method uses the known displacement on the interface to evaluate an interpolated value for the interior vertices of the fluid grid. A great advantage of this method is that it does not need the connectivity of the mesh elements and can be applied to both structured and unstructured grids. The interpolated displacement  $\delta\mathbf{r}$  at a grid vertex  $\mathbf{x}_v$  is evaluated as:

$$\delta\mathbf{r}(\mathbf{x}_v) = \sum_{i=1}^{nv} \gamma_i \varphi(\|\mathbf{x}_v - \mathbf{x}_i\|) \quad (26)$$

where  $nv$  is the number of nodes on the interface  $\mathbf{x}_i$ , and  $\varphi$  is the radial basis function. The Wendland  $C^2$  function [40] is used for  $\varphi$  since it preserves good quality of the dynamic mesh, specially near the moving interface. The weight coefficients  $\gamma_i$  are evaluated using the known displacements on the interface nodes

$$\delta\mathbf{r}(\mathbf{x}_i) = \delta\mathbf{d}(\mathbf{x}_i) \quad i = 1, 2, \dots, nv \quad (27)$$

for  $\mathbf{x}_i \in \Gamma$ . Therefore, the size of the system of equations to obtain the weight coefficients is limited to the number of known points  $nv$ .

Surface velocities are evaluated according to the space conservation law (SCL) which guarantees no volume is lost while moving the grid. For any control volume in the fluid domain, the SCL is stated as:

$$\frac{\partial v}{\partial t} - \int_{cs} \mathbf{w} \cdot d\mathbf{A} = 0 \quad (28)$$

where  $v$  and  $cs$  stand, respectively, for the volume and the boundary surface of a control volume. As before,  $\mathbf{w}$  is the domain velocity and  $\mathbf{A}$  is the area vector pointing outward.

Time rate of change of volume is equal to the sum of volumes swept by each face of a control volume. In this work we evaluate the domain velocity at each face,  $\mathbf{w}_f$ , based on the volume swept by that face. With a second-order backward discretization it reads:

$$\mathbf{w}_f^{n+1} = \frac{3}{2} \left( \frac{\delta v}{A \Delta t} \mathbf{n}_f \right)^{n+1} - \frac{1}{2} \left( \frac{\delta v}{A \Delta t} \mathbf{n}_f \right)^n \quad (29)$$

where  $A$  is the surface area,  $\mathbf{n}_f$  unit normal vector of the face,  $\Delta t$  time step and  $\delta v$  the volume swept by the face at one time step (see Figure 1).

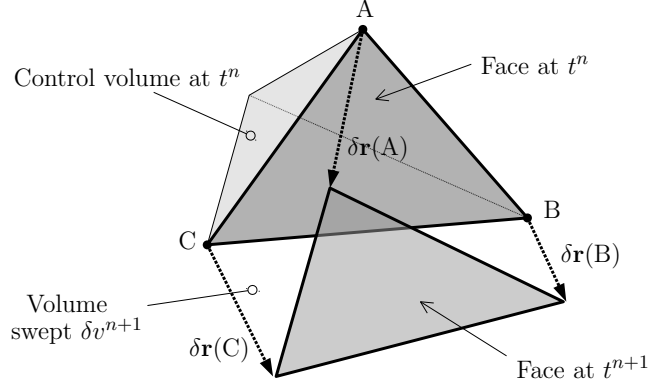


Figure 1: Volume swept ( $\delta v$ ) by each face of an arbitrarily shaped polyhedral. The displacement of each vertex is shown by  $\delta r$ .

More detailed description of the dynamic mesh method could be found in [39, 20]. In the remaining of this paper, we will use the notation  $\mathcal{M}$  to refer to the mesh movement step:

$$(\Omega_f^{n+1}, \mathbf{w}^{n+1}) = \mathcal{M}(\mathbf{d}_\Gamma^{n+1}) \quad (30)$$

#### 3.4. Structural solver

Structural equations are discretized in time using a second-order Newmark method. Defining the structural velocity  $\mathbf{v} = \frac{\partial \mathbf{d}}{\partial t}$ , we update the velocity and displacement of the structure as:

$$\mathbf{v}^{n+1} = \mathbf{v}^n + \frac{\Delta t}{2\rho_s} [\nabla \cdot \mathbf{P}(\mathbf{d}^{n+1}) + \nabla \cdot \mathbf{P}(\mathbf{d}^n)] \quad (31)$$

$$\mathbf{d}^{n+1} = \mathbf{d}^n + \Delta t \mathbf{v}^n + \frac{\Delta t^2}{4\rho_s} [\nabla \cdot \mathbf{P}(\mathbf{d}^{n+1}) + \nabla \cdot \mathbf{P}(\mathbf{d}^n)] \quad (32)$$

In this work we use the structural solver as a black-box module. Any structural solver with a second order temporal accuracy could be used. In

the remaining of this paper, we use the notation  $\mathcal{S}$  to refer to the structural solver as a function of surface stress on the interface:

$$\mathbf{d}_\Gamma = \mathcal{S}(\boldsymbol{\sigma}_\Gamma) \quad (33)$$

where  $\mathbf{d}_\Gamma$  is the location of the interface and  $\boldsymbol{\sigma}_\Gamma$  is the surface stress on the interface exerted by the fluid  $\boldsymbol{\sigma}_\Gamma = \boldsymbol{\sigma}_f(p, \mathbf{u})|_\Gamma \mathbf{n}_\Gamma$ .

### 3.5. Coupled problem

We present a semi-implicit FSI coupling method in which only the pressure term of the fluid is strongly coupled to the structure. The remaining fluid terms as well as the dynamic mesh step are evaluated only once per time step. Using a projection method for fluid equations allows us to effectively segregate the pressure term and couple it implicitly to the structure. Strong coupling of the fluid pressure and structural deformation provides for the stability of the method for FSI problems with strong added-mass effect. Loose coupling of the remaining terms helps to avoid excessive computational cost.

The complete FSI solution method from time step  $t^n$  to  $t^{n+1}$  is as follows:

**step 0:** extrapolation of  $\mathbf{d}_\Gamma$  from previous time steps:

$$\tilde{\mathbf{d}}_\Gamma^{n+1} = 2.5\mathbf{d}_\Gamma^n - 2\mathbf{d}_\Gamma^{n-1} + 0.5\mathbf{d}_\Gamma^{n-2} \quad (34)$$

**step 1:** moving the fluid mesh (*explicitly coupled*):

$$(\Omega_f^{n+1}, \mathbf{w}^{n+1}) = \mathcal{M}(\tilde{\mathbf{d}}_\Gamma^{n+1}) \quad (35)$$

**step 2:** ALE convection-diffusion equation (*explicitly coupled*):

$$\begin{aligned} \frac{\mathbf{u}^* - \mathbf{u}^n}{\Delta t} = & -\left[\frac{3}{2}(\mathbf{c} \cdot \nabla \mathbf{u})^n - \frac{1}{2}(\mathbf{c} \cdot \nabla \mathbf{u})^{n-1}\right] \\ & + \frac{\mu_f}{2\rho_f}(\nabla^2 \mathbf{u}^* + \nabla^2 \mathbf{u}^n) - \frac{1}{\rho_f} \nabla p^{n-1/2} \quad \text{in } \Omega_f^{n+1} \end{aligned} \quad (36)$$

**step 3:** fluid pressure and structural equations (*implicitly coupled, solved iteratively*):

$$\mathbf{n}_\Gamma \cdot \mathbf{u}_\Gamma^* = \mathbf{n}_\Gamma \cdot \left( \frac{3\mathbf{d}_\Gamma^{n+1} - 4\mathbf{d}_\Gamma^n + \mathbf{d}_\Gamma^{n-1}}{2\Delta t} \right) \quad \text{on } \Gamma^{n+1} \quad (37)$$

$$\boldsymbol{\tau}_\Gamma \cdot \mathbf{u}_\Gamma^* = \boldsymbol{\tau}_\Gamma \cdot \left( \frac{3\mathbf{d}_\Gamma^{n+1} - 4\mathbf{d}_\Gamma^n + \mathbf{d}_\Gamma^{n-1}}{2\Delta t} \right) + \frac{\Delta t}{\rho_f} \boldsymbol{\tau}_\Gamma \cdot (2\nabla\phi^n - \nabla\phi^{n-1})|_\Gamma \quad \text{on } \Gamma^{n+1} \quad (38)$$

$$\nabla^2\phi^{n+1} = \frac{\rho_f}{\Delta t} \nabla \cdot \mathbf{u}^* \quad \text{in } \Omega_f^{n+1} \quad (39)$$

$$p^{n+1/2} = p^{n-1/2} + \phi^{n+1} - \frac{\mu_f \Delta t}{2\rho_f} \nabla^2\phi^{n+1} \quad \text{in } \Omega_f^{n+1} \quad (40)$$

$$p^{n+1} = \frac{3}{2}p^{n+1/2} - \frac{1}{2}p^{n-1/2} \quad \text{in } \Omega_f^{n+1} \quad (41)$$

$$\boldsymbol{\sigma}_\Gamma^{n+1} = \boldsymbol{\sigma}_f(p^{n+1}, \mathbf{u}^*)|_{\Gamma \cap \Omega} \quad \text{on } \Gamma^{n+1} \quad (42)$$

$$\mathbf{d}_\Gamma^{n+1} = \mathcal{S}(\boldsymbol{\sigma}_\Gamma^{n+1}) \quad \text{on } \Gamma^{n+1} \quad (43)$$

**step 4:** velocity correction (*explicitly coupled*):

$$\mathbf{u}^{n+1} = \mathbf{u}^* - \frac{\Delta t}{\rho_f} \nabla\phi^{n+1} \quad \text{in } \Omega_f^{n+1} \quad (44)$$

$$\mathbf{u}_\Gamma^{n+1} = \frac{3\mathbf{d}_\Gamma^{n+1} - 4\mathbf{d}_\Gamma^n + \mathbf{d}_\Gamma^{n-1}}{2\Delta t} \quad \text{on } \Gamma^{n+1} \quad (45)$$

Every time step starts with predicting the location of the interface by means of an extrapolation from previous time steps. The fluid mesh is then moved to adapt to the predicted location of the interface (step 1). Therefore, the geometrical nonlinearities are treated explicitly. The convection-diffusion equation in step 2 is also solved only once per time step. Step 3 is the implicit part of the coupling in the above algorithm where fluid pressure is strongly coupled to the structural deformation. Equations in step 3 are solved together (iteratively). This step provides for the stability of the method for FSI problems with strong added-mass effect. Note that the current structural deformation  $\mathbf{d}_\Gamma^{n+1}$  is used in Eq. (37) and (38), while it is evaluated in Eq. (43), which shows the implicit coupling between the equations in step 3.

A Newton-Krylov method with approximated Jacobian [20] is used to carry out the coupling iterations in step 3.

As seen in the Eq. (37) and (38), the kinematic equilibrium on the interface is applied on the predicted velocity field (in a corrected consistent manner) during the coupling iterations. The predicted velocity is also used to evaluate the shear stress term in Eq. (42). When the convergence is achieved for the iterative process in step 3, the velocity field is corrected using the converged field  $\phi^{n+1}$  and the coupling condition is applied on the final velocity (step 4).

### 3.6. Temporal accuracy

An error analysis is required to evaluate the temporal accuracy of the proposed method in a FSI problem. Analytical and numerical analysis could be used for this purpose. Analytical energy and error estimates have been used in some previous studies to evaluate stability and order of convergence of FSI methods (e.g. [14, 34]). However, these analyses were limited to a simplified linear system of equations (Stokes equations for fluid and a lower dimensional, linear elastic model for structure). The non-linear term in fluid equations represents an important physical aspect and also changes the mathematical characteristics of the governing equations. The non-linear term in solid equations has a similar importance. Evaluating the error bound and convergence rate of numerical methods applied to realistic FSI problems normally rely on numerical experiments.

In this study numerical tests are carried out on three widely used FSI test cases to demonstrate the second-order accuracy of the proposed method. For that purpose, test solutions are carried out using increasingly larger time steps and their error is evaluated at a certain point in time. The spatial grid is kept constant for all the test solutions. In the lieu of an exact solution, reference numerical results are generated for each test case, using a very small time step size and identical spatial grid. Test solutions are compared to the reference solution to evaluate the error for each variable. The errors with respect to the reference solution are evaluated at each spatial point and presented in both  $L_2$  and  $L_\infty$  norms. The temporal order of accuracy is determined by evaluating the slope of the graph of error against time step size, in a logarithmic scale.

It should be noted that the global error contains both spatial and temporal components and behaves, in general terms, as  $O(\Delta x^a + \Delta t^b)$ , where  $\Delta x$  and  $\Delta t$  are the spatial grid size and time step, respectively. The powers  $a$  and

$b$  are, respectively, the asymptotic orders of spatial and temporal accuracy. In order to evaluate the asymptotic order of temporal accuracy, the spatial component of the error must be kept considerably smaller than the temporal component to make sure it does not affect the error analysis results. When the errors are evaluated with respect to an exact (analytical) solution ( $\mathcal{X}_e$ ), it means the spatial grid should be sufficiently fine to assure a small spatial error. Ideally one may have  $\Delta x \ll \Delta t^{b/a}$  so that the error could be approximated as  $O(\Delta t^b)$ . In our numerical tests, reference numerical results ( $\mathcal{X}_r$ ) are used instead of an exact solution, due to the lack of exact solution for the realistic problems considered. The reference solution is obtained using a certain spatial and temporal grid size ( $\Delta x_r$  and  $\Delta t_r$ ), thus itself contains an error with respect to the exact solution,  $\epsilon_r = \mathcal{X}_r - \mathcal{X}_e$ . Test solutions ( $\mathcal{X}_t$ ) are obtained by using different (and increasingly larger) time step sizes but an identical spatial grid. Therefore, In comparing the test results to the reference results, the error due to the spatial discretization is discarded since it is identical for the test and reference solutions.

To further clarify the aforementioned explanation, let us assume the global error (with respect to the exact solution) to be of the form  $O(\Delta x^a + \Delta t^b) = O_1(\Delta x^a) + O_2(\Delta t^b)$ . We expect  $a = b = 2$  for the method in this work. The error of the reference solution with respect to the exact solution is then  $\epsilon_r = O_1(\Delta x_r^a) + O_2(\Delta t_r^b)$ . Similarly, the error (with respect to the exact solution) of the test solutions using test time step size  $\Delta t$  and identical spatial grid is  $\epsilon_t = O_1(\Delta x_r^a) + O_2(\Delta t^b)$ . When we compare the test results to the reference results and evaluate the error with respect to the reference solution, the error for each test solution becomes  $\epsilon = \mathcal{X}_t - \mathcal{X}_r = O_2(\Delta t^b) - O_2(\Delta t_r^b)$ , because the spatial error is identical for test and reference solutions. In the numerical tests, we have used a much smaller time step size for the reference results ( $\Delta t_r \ll \Delta t$ ). Therefore, the error with respect to the reference solution becomes  $\epsilon \approx O_2(\Delta t^b)$ . Thus, by evaluating the error with respect to the reference solution, for different time step sizes, one is able to appropriately asses the temporal accuracy of the method. In the numerical tests, graphs of error against time step size ( $\epsilon - \Delta t$ ) are presented that show a slope of two, which suggest a second-order temporal accuracy according to the above explanation.

It should be also noted that our numerical tests would have revealed a mixed error term of the form  $O(\Delta x \Delta t)$ . If there existed such a term in the global error (in this work it would be  $O_1(\Delta x^2) + O_2(\Delta t^2) + O_3(\Delta x \Delta t)$ ), the error with respect to the reference solution would become  $\epsilon = O_2(\Delta t^b) -$

$O_2(\Delta t_r^b) + O_3(\Delta x_r \Delta t) - O_3(\Delta x_r \Delta t_r)$ . Since we have kept the spatial grid constant for the analysis, and the fact that lower order error is the dominant term, we would have  $\epsilon \approx O_3(\Delta t)$ . This means the slope of the error graphs in the numerical tests would become unity and reveal if a mixed error term existed in the solution.

## 4. NUMERICAL TESTS

In this section, numerical results on benchmark FSI problems are presented to study the accuracy of the proposed method. Three FSI test cases are considered, as well as a test case that contains only fluid flow. The three FSI cases vary widely, featuring an internal flow contained by a deformable membrane, an external flow over a blunt body with rigid-body motion, and a cavity flow with a deformable bottom. Obtained results are compared to experimental and numerical results from the literature in order to validate the solution method. An error analysis is provided for each test case that demonstrates second-order temporal accuracy of the solution.

### 4.1. Lid-driven cavity (only fluid flow)

As the first numerical test case, we study the flow inside a classical lid-driven cavity at  $Re = 400$ . The problem is a  $1\text{m} \times 1\text{m}$  cavity with the lid moving at a constant velocity of  $u_1 = 1\text{m/s}$ . The fluid density and viscosity are  $\rho_f = 1.0\text{ kg/m}^3$  and  $\mu_f = 0.0025\text{ Pa}\cdot\text{s}$ , respectively. All the walls are rigid and there is no fluid-structure interaction.

A classical  $31 \times 31$  mesh is used to solve the problem. A finer grid of  $61 \times 61$  is also used for comparison. Spatial discretization is carried out using a finite volume method with a second-order central scheme. Figure 2 compares the steady state solution for horizontal velocity on the vertical mid-line ( $x = 0.5$ ), against the classical results of Kim and Moin (1985) [38]. The steady state was reached after roughly 30 seconds ( $t > 30\text{s}$ ). As seen in figure 2, the results obtained by the coarse and fine mesh are almost indistinguishable and they agree very well with those of Kim and Moin (1985) [38].

To evaluate the temporal accuracy of the method, four different time step sizes are used to solve the problem from  $t = 0$  till  $t = 1\text{s}$  and the error is evaluated at  $t = 1\text{s}$ . The time step ranges from  $5 \times 10^{-4}$  to  $4 \times 10^{-3}\text{s}$ . In the lieu of an exact solution, reference results are generated using a much smaller time step size of  $\Delta t = 5 \times 10^{-5}\text{s}$ . The reference time step size is an order of magnitude smaller than the smallest test time step. The spatial grid is

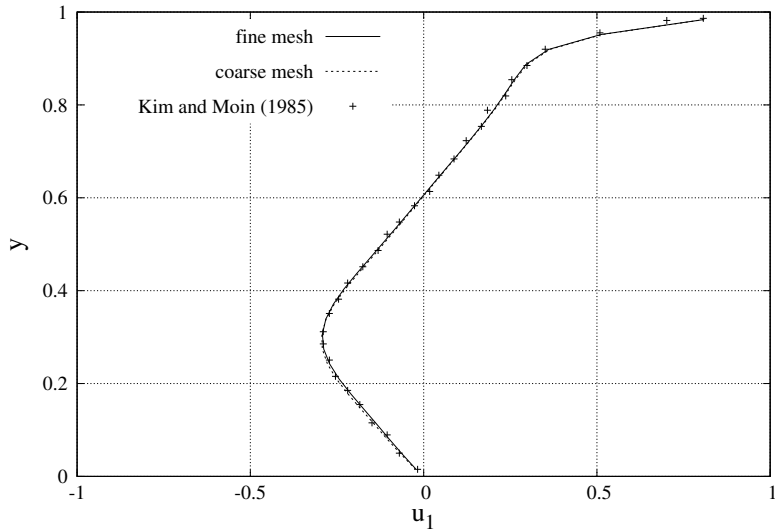


Figure 2: Horizontal component of velocity on the vertical mid-line of a lid-driven cavity (NO FSI) in the steady state.

kept constant for the tests. The error with respect to the reference solution is evaluated at every grid point and presented in both  $L_2$  and  $L_\infty$  norms in figure 3, on a logarithmic scale. A solid line with a slope of two ( $\Delta t^2$ ) is also plotted to compare the slope of the error graphs. A slope of two of the error graphs means the rate of convergence of the error by time step size is two, i.e. a second-order accuracy.

As seen in figure 3, both velocity and pressure are clearly second-order accurate. To monitor closely the error of the pressure on the domain boundaries, the error on the boundaries is evaluated separately and plotted in figure 3. It demonstrates that the proposed method solves the fluid equations with a second-order accuracy up to the domain boundary.

#### 4.2. Driven cavity with deformable bottom

Numerical tests are carried out on a benchmark problem studied in [8, 41], among others. The test case is a 2-D driven cavity of  $1\text{m} \times 1\text{m}$  with a flexible bottom wall. The top boundary of the cavity is moving with an oscillatory speed of  $u(t) = 1 - \cos(\omega t)$  m/s, with  $\omega = 2\pi/5$ . There are two openings of 0.1m length on the sidewalls that allow the fluid to enter to and exit from the domain. Figure 4(left) shows a schematic description of the

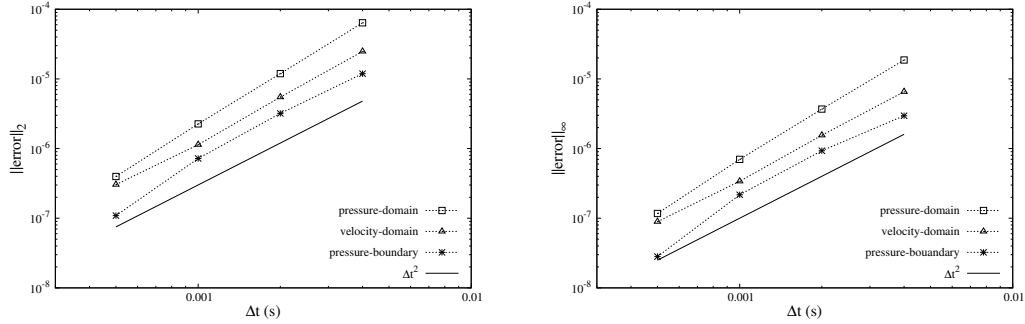


Figure 3: Variation of relative error inside the domain and on the boundaries by time step size, driven cavity case (NO FSI). Left:  $L_2$  norm; Right:  $L_\infty$  norm.

problem. The fluid density and viscosity are  $\rho_f = 1.0 \text{ kg/m}^3$  and  $\mu_f = 0.01 \text{ Pa}\cdot\text{s}$ , respectively. The flexible structure at the bottom has a thickness of  $h = 0.05\text{m}$ , the structural density is  $\rho_s = 5 \text{ kg/m}^3$  and the Young modulus  $E = 250 \text{ N/m}^2$ .

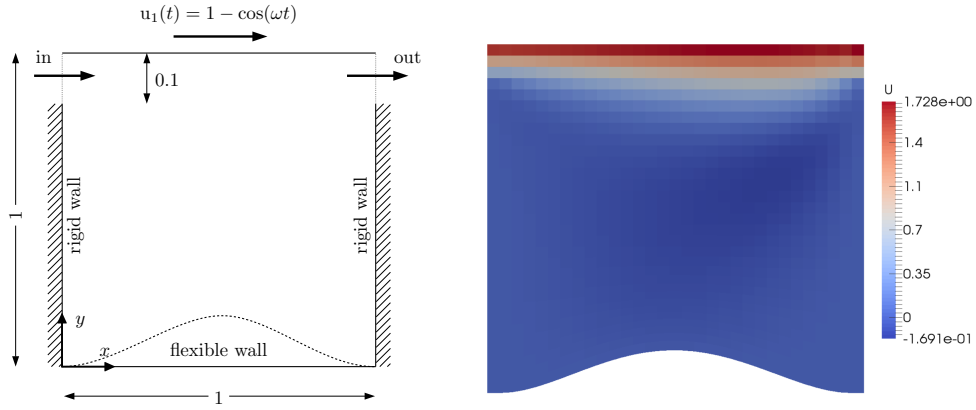


Figure 4: Driven cavity with flexible bottom. Left: schematic view of the domain and problem setup; Right: contour plot of horizontal velocity  $u_1(\text{m/s})$  inside the deformed domain at  $t = 7\text{s}$ .

The flexible bottom is modeled as an Euler-Bernoulli beam, governed by the following equation:

$$\rho_s A \frac{\partial^2 \mathbf{d}}{\partial t^2} + EI \frac{\partial^4 \mathbf{d}}{\partial x^4} = q(x, t) \quad (46)$$

where  $\mathbf{d} = [0, y, 0]^T$  in a Cartesian coordinate  $(x, y, z)$ ,  $A$  is the cross section

area of the beam,  $I$  the second moment of area, and  $q$  is the load per unit length.

A  $100 \times 100$  spatial grid with refinement near the bottom wall is used to solve the problem. Spatial discretization is carried out using a finite volume method with a second-order central scheme. The structure is a thin membrane so the fluid mesh elements on the interface are also used as the computational grid for the structural equations. Thus, the structural grid nodes match the fluid mesh on the interface and there is no need for interpolation of parameters between the domains. Figure 4(right) shows the flow field inside the domain with structural deformation at the bottom, at  $t = 7$ s.

To evaluate the temporal accuracy of the method, the problem is solved using four different time step sizes ranging from  $5 \times 10^{-4}$  to  $4 \times 10^{-3}$ s. Reference results are obtained using a much smaller time step of  $\Delta t = 5 \times 10^{-5}$ s. The spatial grid is kept constant for the tests. The simulations are carried out from  $t = 0$  until  $t = 1$ s, and the error is evaluated at  $t = 1$ s. The error is evaluated at every grid node and presented in both  $L_2$  and  $L_\infty$  norms.

Figures 5 and 6 represent the variation of the relative error with time step size  $\Delta t$  in logarithmic scales. Figure 5 represents the error of fluid velocity and pressure inside the fluid domain, while Figure 6 represents the error of fluid pressure and structural deformation on the fluid-structure interface. Results demonstrate a clear second-order temporal accuracy for all the variables of interest in both  $L_2$  and  $L_\infty$  norms.

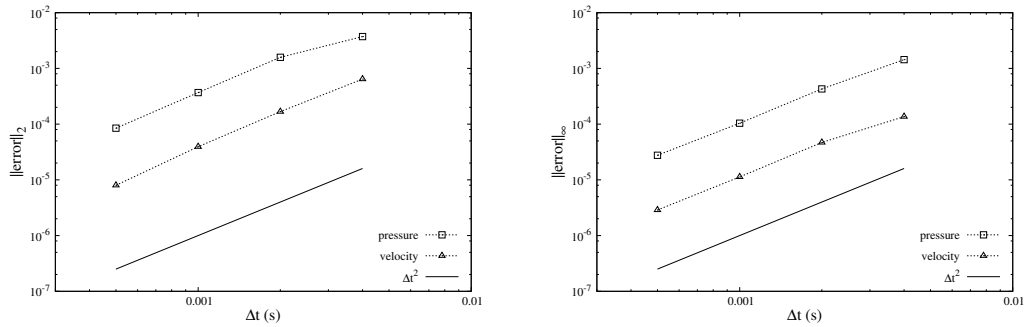


Figure 5: Variation of relative error inside the fluid domain by time step size, driven cavity with flexible bottom. Left:  $L_2$  norm; Right:  $L_\infty$  norm.

#### 4.3. Wave propagation in a 2-D deformable channel

This test case is to simulate the propagation of pressure waves inside a 2D straight channel with elastic walls. The problem is similar to blood flow

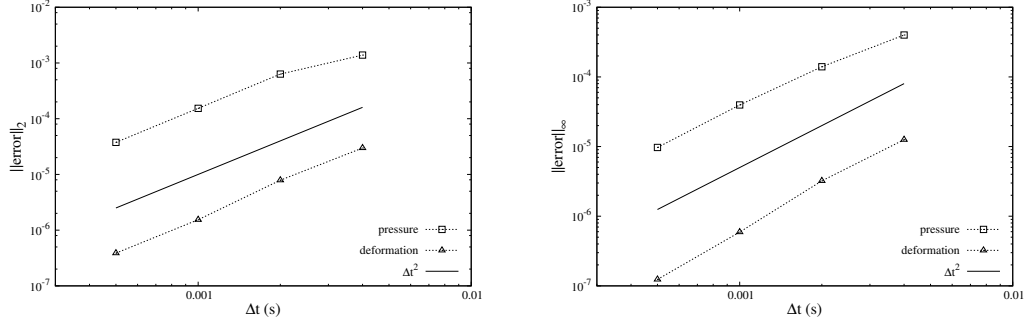


Figure 6: Variation of relative error on the fluid-structure interface by time step size, driven cavity with flexible bottom. Left:  $L_2$  norm; Right:  $L_\infty$  norm.

inside large arteries and was studied, among others, in [42, 14, 43, 44]. The problem represents a strong added-mass effect, as the densities of the fluid and the structure are very similar and the domain is slender.

The initial fluid domain is  $[0, L] \times [0, R_0]$ , where  $L = 6\text{cm}$  is the length of the channel and  $R_0 = 0.5\text{cm}$  is its height. The top boundary is an elastic wall interacting with the fluid, while the bottom boundary is a slip wall (axis of symmetry). Fluid pressure is specified at both inlet and outlet boundaries, while Neumann boundary condition is used for velocity. Pressure at the outlet boundary is set to zero while the inlet pressure represents a time-dependent pulse:

$$P_{inlet}(t) = \begin{cases} P_{pulse} \sin(\pi t / t_{pulse}) & 0 \leq t \leq t_{pulse} \\ 0 & t > t_{pulse} \end{cases}$$

where  $P_{pulse} = 2000\text{Pa}$  and  $t_{pulse} = 0.005\text{s}$  are, respectively, the amplitude and duration of the pressure pulse.

The deformable wall is modeled using the generalized string model [45]:

$$\rho_s h \frac{\partial^2 \mathbf{d}}{\partial t^2} - \frac{Eh}{2(1+\nu)} \frac{\partial^2 \mathbf{d}}{\partial x^2} + \frac{Eh}{1-\nu^2} \frac{\mathbf{d}}{R_0^2} + \alpha_0 \rho_s h \frac{\partial \mathbf{d}}{\partial t} - \frac{\alpha_1 Eh}{2(1+\nu)} \frac{\partial^3 \mathbf{d}}{\partial x^2 \partial t} = q(x, t) \quad (47)$$

where the solid density is  $\rho_s = 1100\text{kg/m}^3$ , the Young modulus  $E = 7.5 \times 10^4\text{N/m}^2$ , the wall thickness  $h = 0.1\text{cm}$ , the Poisson ratio is  $\nu = 0.5$ , and the damping parameters  $\alpha_0 = 1$  and  $\alpha_1 = 0.001$ . Fluid density and viscosity are  $\rho_f = 1000\text{kg/m}^3$  and  $\mu_f = 0.0035\text{Pa}\cdot\text{s}$ , respectively. The system is at rest at  $t = 0$  and the simulations are carried out till  $t = 0.015\text{s}$ .

Three different spatial and temporal grid resolutions (table 1) are used to solve the problem, in order to ensure the grid independency of the results. Fluid mesh is refined near the top boundary (F-S interface) using a hyperbolic function. The boundary nodes for the fluid mesh coincide with the grid nodes for the solid domain, thus there is no need for further interpolations between the domains.

Table 1: Three grid resolutions used for deformable channel case.

Mesh name	No. of nodes		time step
	length	height	$\Delta t$ (s)
coarse	100	20	2e-5
medium	150	30	1e-5
fine	200	40	5e-6

Figure 7 depicts the location of the interface at  $t = 0.015s$ , evaluated using the three grid resolutions mentioned in table 1. As seen in the figure 7, the results with medium and fine meshes are almost indistinguishable, which means the mesh convergence is achieved.

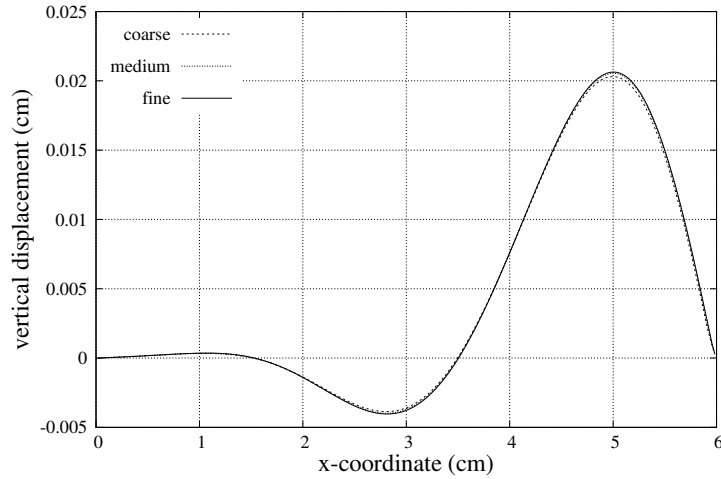


Figure 7: Displacement of the elastic boundary at  $t = 0.015s$ , evaluated with different grid resolutions.

Figure 8 contains contour plots of pressure at three different instants,

demonstrating the propagation of the wave inside the channel. The deformation of the channel wall (although small) is also visible in the figure. Despite the fluid being incompressible, the pressure wave propagates with a finite velocity, which is an important feature of this problem.

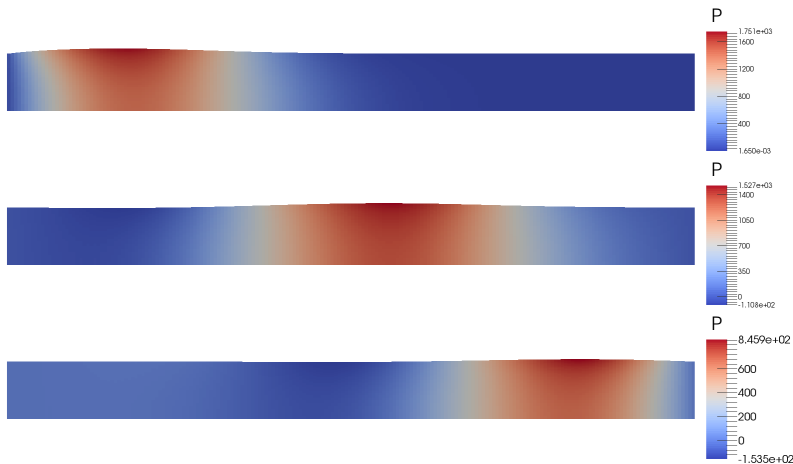


Figure 8: Propagation of pressure wave inside the deformable channel, contour plots of pressure at  $t = 0.005s$ ,  $t = 0.01s$  and  $t = 0.015s$ .

To evaluate the accuracy of the results and verify the presented numerical methodology, a comparison to other numerical results in [43, 44] has been carried out. Figure 9 shows the location of the interface at  $t = 0.015s$  evaluated with the medium mesh and  $\Delta t = 1 \times 10^{-5}s$ , together with the results from Fernandez et al. [43] and Li et al. [44]. As seen in the figure, our results agree fairly well with those of the other reports. There is a slight difference between the three sets of results which is acceptable considering they use different discretizations and FSI coupling techniques. It is worth to mention that results in [43] are evaluated using a first-order method and a very small time step  $\Delta t = 1 \times 10^{-6}s$ . Results of simulations with different time step sizes (and different spatial mesh) are also reported in [43] to show the convergence to a limiting solution (similar to figure 7). These results show that convergence is achieved at  $\Delta t = 1 \times 10^{-6}s$  and for larger time steps there is a considerable discrepancy (see section 4.1 in [43]). However, our method provides time-step-independent results for  $\Delta t = 1 \times 10^{-5}s$  (figure 7). This fact highlights the advantage of using higher-order methods. Unfortunately in [44] the time step size for this test case is not mentioned.

To evaluate the temporal accuracy of the method, the problem was solved

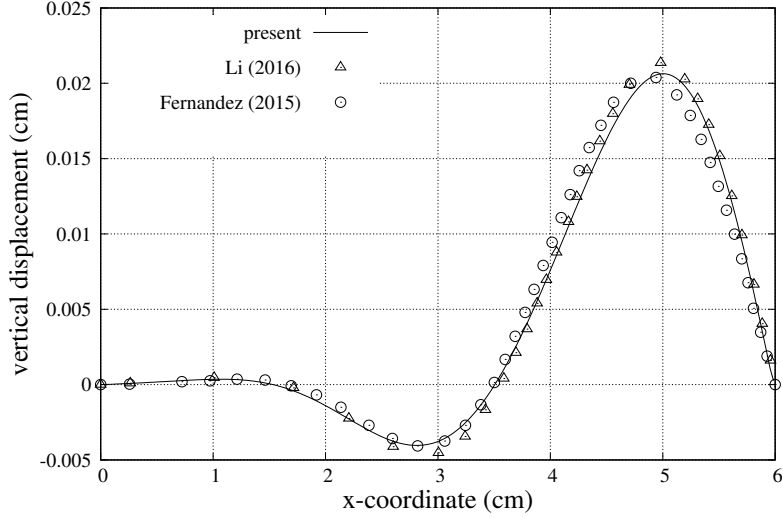


Figure 9: Displacement of the elastic boundary at  $t = 0.015\text{s}$ , comparison with numerical results at [43, 44].

with four different time step sizes between  $5 \times 10^{-5}$  to  $4 \times 10^{-4}\text{s}$ . Reference results were generated using  $\Delta t = 5 \times 10^{-6}\text{s}$ , which is an order of magnitude smaller than the smallest test time step size. The spatial grid is kept constant for the analysis. The error for each time step size was evaluated and is presented in figures 10 and 11. These results demonstrate a clear second-order temporal accuracy for all the variables of interest, in both  $L_2$  and  $L_\infty$  norms.

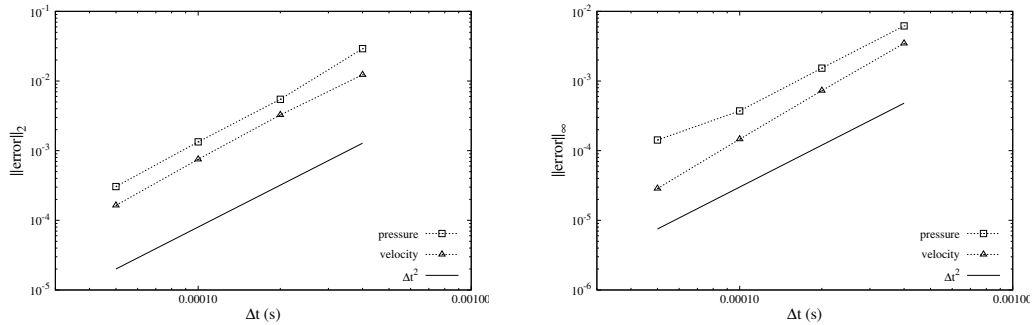


Figure 10: Variation of relative error in the fluid domain by time step size, elastic channel case. Left:  $L_2$  norm; Right:  $L_\infty$  norm.

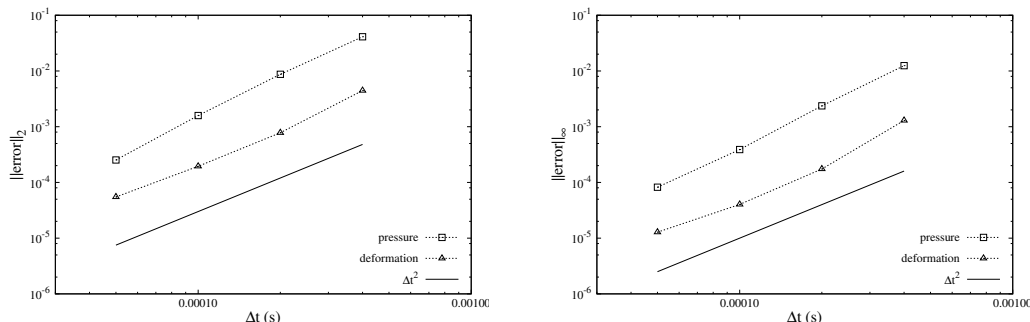


Figure 11: Variation of relative error on the fluid-structure interface by time step size, elastic channel case. Left:  $L_2$  norm; Right:  $L_\infty$  norm.

#### 4.4. Vortex-induced vibration of a circular cylinder

For this test case, the fluid flow over an elastically-mounted cylinder is solved in order to study the structural vibration due to the flow vortices. Vortex-induced vibration (VIV) is an important class of FSI problems with a wide range application. The cylinder is elastically mounted and it can move as a rigid-body around its reference position. Due to the vortex-shedding over the blunt body, the flow exerts an oscillating force on the cylinder, which causes it to vibrate. Generally, the vortex-shedding over an elastically-mounted cylinder occurs at the same frequency as for a fixed cylinder (the Strouhal frequency). However, there is a certain range of Reynolds number where the vortex-shedding frequency changes to match the natural structural frequency of the cylinder. This range of Reynolds number is called *lock-in* region as the vortex-shedding no longer occurs at the Strouhal frequency, but at the natural frequency of the solid.

A series of VIV simulations are carried out to numerically reproduce the experimental results of Anagnostopoulos and Bearman [46]. A rectangular fluid domain is considered around a circular cylinder with a diameter  $D$ . The size of the domain is chosen based on previous experience of the authors and guidance from other VIV studies in the literature. Figure 12 depicts the layout of the domain and the problem setup. The flow enters the domain with a uniform velocity  $U_\infty$ , while the pressure is set to zero at the outlet. For the sake of computational efficiency, the ALE formulation and the dynamic mesh is limited to a circular zone around the cylinder with a diameter of  $6D$ . The mesh is not moving at the rest of the domain and an Eulerian formulation is used. The cylinder motion is constrained to the cross-flow direction only, as

per experiments.

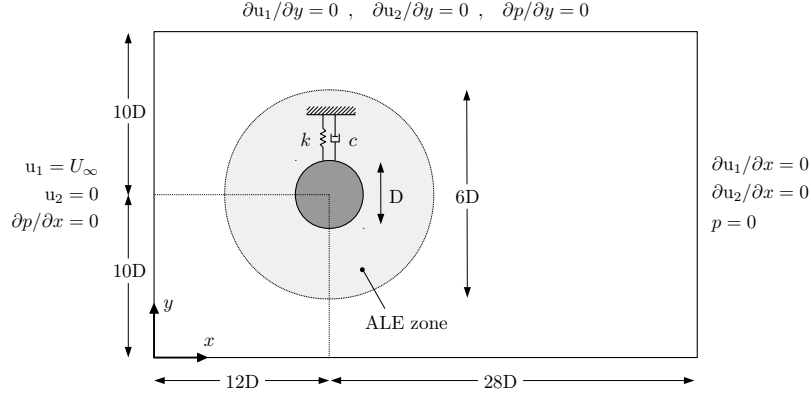


Figure 12: Schematic view of the domain and problem setup for the VIV test case.

The rigid-body motion of the cylinder is modeled as a system of spring and damper:

$$m \frac{\partial^2 \mathbf{d}}{\partial t^2} + c \frac{\partial \mathbf{d}}{\partial t} + k \mathbf{d} = q(t) \quad (48)$$

where  $\mathbf{d} = [0, y, 0]^T$ ,  $y$  being the vertical location of the center of the cylinder. The cylinder mass is shown by  $m$ ,  $c$  is the damping coefficient,  $k$  the spring stiffness, and  $q(t)$  stands for the vertical component of the time-variant forces exerted on the cylinder by the fluid flow. The natural frequency of the vibration system is  $f_n = \frac{1}{2\pi} \sqrt{\frac{k}{m}}$ . Table 2 shows the definition of the relevant non-dimensional numbers for this problem and their respective values. All non-dimensional numbers are equal to those of the experiments [46]. The Reynolds number varies between 90 to 140 and the associated reduced velocity between 5.01 to 7.80. The variable  $l$  in the definition of mass ratio is the length of the cylinder.

To assess the grid-independency of the results, three different grids are used to solve the problem at  $Re=110$ , which lies in the lock-in zone as seen later. Table 3 contains the information of the mesh and three representative values of the results, i.e. the normalized amplitude of the vibrations  $A^* = y_{max}/D$ , vortex-shedding frequency  $f$ , in non-dimensional form  $fD/U_\infty$ , and the mean drag coefficient  $\bar{C}_d$ . The mean drag coefficient is the time average of the instantaneous drag coefficient  $C_d$  from  $t = 1000s$  until  $t = 5000s$ ,

Table 2: Relevant non-dimensional numbers of the VIV problem and their value.

Name	Definition	Value
Reynolds (Re)	$\rho_f U_\infty D / \mu_f$	90-140
Reduced velocity ( $U_r$ )	$U_\infty / (f_n D)$	5.01-7.80
Mass ratio	$\rho_f D^2 l / 2m$	0.00427
Damping ratio	$c / 2\sqrt{km}$	0.0012

where a periodic solution exists. The drag coefficient itself is defined as  $C_d = \frac{F_D}{\frac{1}{2}\rho_f U_\infty^2 D}$ , where  $F_D$  is the drag force defined as the x-component of the total force applied on the solid boundary  $F_D = \mathbf{n}_x \cdot \int_\Gamma \boldsymbol{\sigma}_f \mathbf{n}_\Gamma d\Gamma$ .

Table 3: mesh-independency of VIV results at Re=110.

Mesh name	No. of cells	$A^*$	$fD/U_\infty$	$\overline{C_d}$
coarse	7195	0.417	0.165	1.43
medium	13685	0.408	0.163	1.53
fine	27091	0.410	0.163	1.56

Results in Table 3 show that the medium and fine grids yield similar results. We have used the medium mesh to conduct further simulations, for the sake of both accuracy and computational efficiency. Grid-independence study at one Reynolds number is sufficient for this test case because the range of studied Reynolds number is small ( $90 \leq Re \leq 140$ ).

Figure 13 demonstrates contour plots for pressure inside the domain at two different instants while the cylinder is locked-in ( $Re = 110$ ) and undergoes large-amplitude vibrations. The structure of the wakes and vortices could be seen at the rear of the cylinder. Results of the simulations for the range of Reynolds number in table 2 are presented in figure 14, along with experimental data from [46] and other numerical results from [47, 48, 25]. The compared results are the normalized amplitude of the vibrations ( $A^*$ ), and the vortex-shedding frequency divided by the natural frequency of the structure ( $f/f_n$ ).

It is seen in figure 14 that the lock-in phenomenon is well captured. For Reynolds numbers  $Re < 95$  and  $Re > 115$  the vortex shedding occurs at the

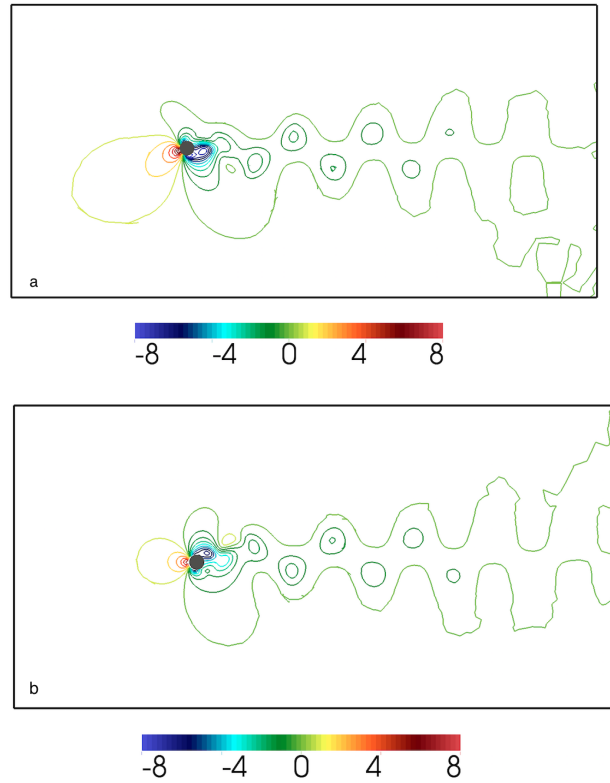


Figure 13: Contour plots of pressure (color legend in Pa) inside the domain at two instants while the cylinder undergoes large-amplitude vibration. a: cylinder approximately at the equilibrium point ( $y = 0$ ); b: cylinder approximately at the maximum displacement ( $y = -0.4D$ )

Strouhal frequency (frequency of vortex-shedding over a fixed cylinder at the same Reynolds number). In this range of Reynolds number, the amplitude of the vibration is small. The lock-in region is at  $95 < Re < 115$ , where the amplitude of the vibration is significantly larger. In the lock-in zone, the vortex shedding no longer occurs at the Strouhal frequency, but at the natural frequency of the cylinder.

Results in figure 14 agree fairly well with the experimental and numerical results from the literature. Different numerical results in the figure differ fairly amongst each other, which is due to the use of different numerical methods and complexity of the problem. Assessing the present results, it is seen that the predicted amplitude of vibration is smaller than the experiments

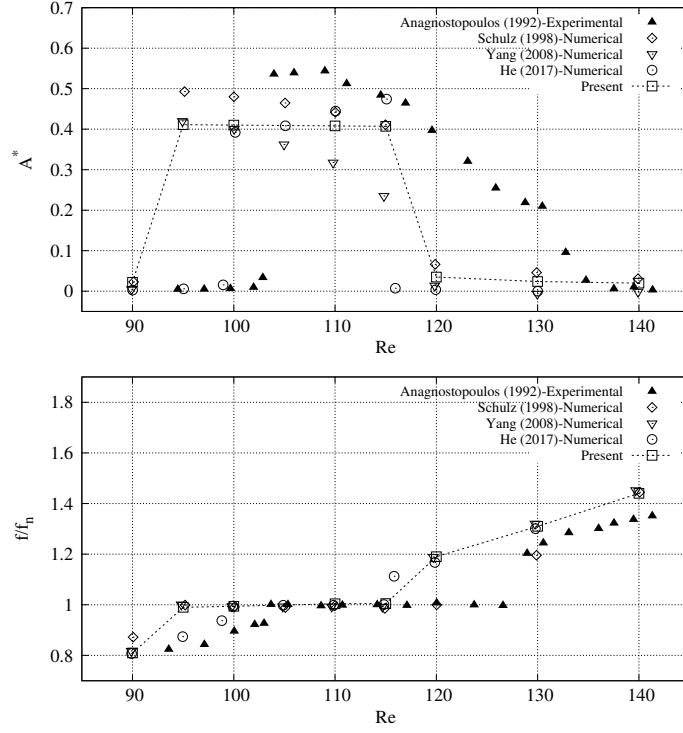


Figure 14: Comparison of the VIV simulation results against experimental and numerical results from the literature. Up: normalized amplitude of vibration; Down: vortex-shedding frequency divided by natural frequency of the cylinder.

but similar to other numerical results. Moreover, there is a slight shift of the location of the lock-in zone, i. e. numerical lock-in region starts and ends at lower Reynolds numbers than its experimental counterpart. This shift is seen in other numerical results as well [47, 48, 25]. The discrepancies may originate from the 3D effects in the experiments, as also noted in [47]. In the experimental study, the authors mention that no end plates were used on the cylinder [46]. This would possibly introduce some 3-D effects that a 2-D simulation like the current work is not able to capture. Moreover, the Reynolds number is close to the region of transition to 3-D (transition to 3-D occurs at about  $Re=180$  for a fixed cylinder). Therefore, it is possible that the Reynolds number locally exceeded the transition range and some 3-D effects were introduced.

Similar to the previous test cases, we have used four time step sizes, ranging from  $8 \times 10^{-3}$  to  $1 \times 10^{-3}$ s, and a much smaller time step of  $1 \times 10^{-4}$ s

for the reference results. The variation of the error by time step size is presented in figures 15 and 16. These results are similar to the previous test cases and further confirm the second-order accuracy of the method.

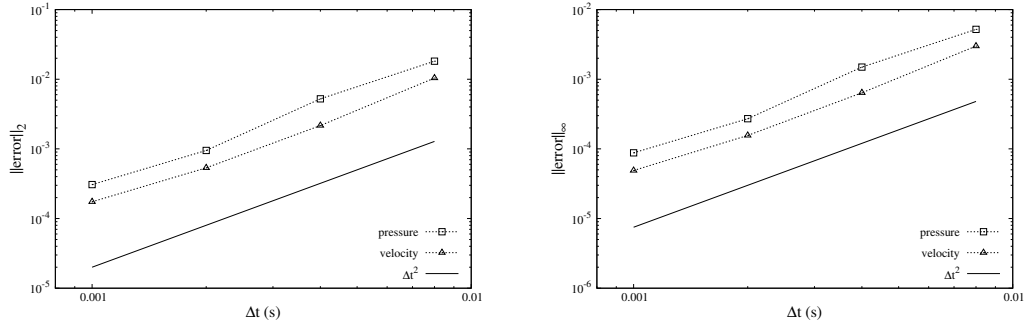


Figure 15: Variation of relative error in the fluid domain by time step size, VIV case. Left:  $L_2$  norm; Right:  $L_\infty$  norm.

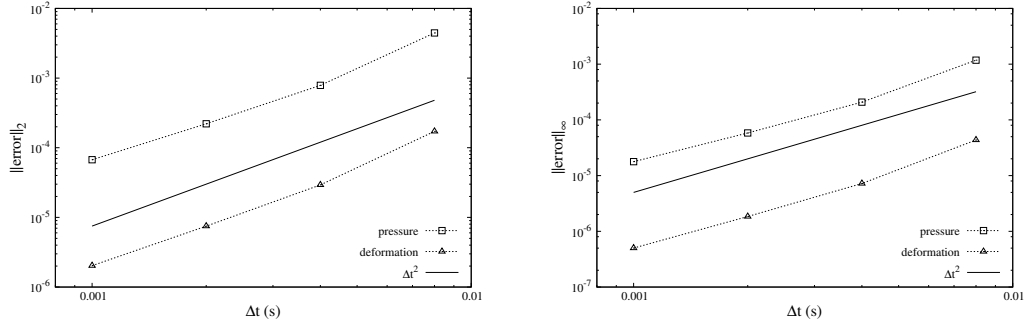


Figure 16: Variation of relative error on the fluid-structure interface by time step size, VIV case. Left:  $L_2$  norm; Right:  $L_\infty$  norm.

## 5. CONCLUSIONS

A second-order semi-implicit method for partitioned solution of fluid-structure interaction problems is proposed. The method uses a second-order projection method to solve the fluid equations and also as a framework for the FSI coupling. The fluid pressure term is effectively segregated using the projection method and is strongly coupled to the structure via Newton iterations. Implicit treatment of the fluid pressure provides for the stability of the method

for FSI problems with strong added-mass effect. The remaining fluid terms and the geometrical nonlinearities (moving mesh) are treated explicitly and thus evaluated only once per time step.

An ALE formulation with a conforming mesh technique is used to solve the fluid flow in a moving domain. A dynamic mesh technique based on radial basis function interpolation method is used to adapt the fluid mesh to the structural displacement. The geometrical terms arisen from the ALE formulation are evaluated with a second-order temporal accuracy. Consistent boundary conditions are developed for the intermediary fields encountered when solving the fluid equations with a projection method. Particular attention is paid to second-order accuracy of the fluid pressure up to the moving boundary.

Second-order accuracy of the method for fully coupled non-linear FSI problems is demonstrated through rigorous numerical tests. Three FSI test cases are considered, including internal flow contained by a deformable membrane, external flow over an elastically-mounted blunt body, and cavity flow with deformable bottom wall. Simulation results are validated against experimental and numerical results from the literature. Different time step sizes are used to solve the problems and the error is evaluated with respect to a reference numerical solution. Second-order temporal accuracy for all the variables of interest (fluid velocity and pressure, and structural displacement) is clearly demonstrated.

## **6. Acknowledgement**

This work was financially supported by the Ministerio de Economía y Competitividad, Secretaría de Estado de Investigación, Desarrollo e Innovación, Spain (ENE2017-88697-R), and a FI PhD scholarship by the Agència de Gestió d'Ajuts Universitaris i de Recerca (AGAUR) of Generalitat de Catalunya.

## **7. Appendix 1. Integral form of the equations and the spatial discretization**

In the paper the governing equations are presented in their differential form and the semi-discretization of the equations in time is described, independent of the choice for discretization in space. This time-discretized equations could then be used with different spatial discretizations. For the sake of completeness, the spatial discretization method used in this work and

the integral form of the conservation equations are described here. We only explain the discretization for the fluid equations in ALE form, as the structural equations are used in their standard Lagrangian form. This annex is complementary to the main text and follows the same notation and nomenclature. The subscript  $f$  used in the main text to refer to the fluid properties is dropped here (e.g.  $\rho_f$  in the main text is simply shown by  $\rho$  here).

We use a finite-volume method with collocated mesh arrangement for space discretization. This method is based on the discretization of the computational domain into a finite number of non-overlapping control volumes (CVs). Each CV has an associated grid node  $P$  located at its centroid where the equations are solved. Each CV has a volume  $v$ , surrounded by a control surface  $s$ , which consists of an arbitrary number of well-defined neighbouring faces. Quantities associated to a grid node (or cell center) are indicated by capital subscripts (e.g.  $P$  or  $N$ ), while the values at the faces are indicated by lower-case subscripts (e.g.  $pn$  to refer to the face located between cell nodes  $P$  and  $N$ ). The area vector of a face is referred to as  $\mathbf{A}_{pn}$  ( $\mathbf{A}_{pn} = A_{pn}\mathbf{n}_{pn}$  where  $A_{pn}$  is the surface area of the face and  $\mathbf{n}_{pn}$  is the normal vector pointing outwards). In this work we use an ALE method on a moving mesh which means the shape and volume of the CVs are varying in time ( $v = v(t)$  and  $s = s(t)$ ). Therefore, the equations of conservation of mass and momentum are integrated over time-varying CVs. The integral form of the governing equations are as follows:

$$\frac{d}{dt} \int_v \rho dv + \int_s \rho(\mathbf{u} - \mathbf{w}) \cdot d\mathbf{A} = 0 \quad (49)$$

$$\frac{d}{dt} \int_v \rho \mathbf{u} dv + \int_s \rho \mathbf{u}(\mathbf{u} - \mathbf{w}) \cdot d\mathbf{A} = \int_s \boldsymbol{\sigma} \cdot d\mathbf{A} \quad (50)$$

The time change of the CV is taken into account in both mass and momentum equations. The change of volume of each CV is present in the transient terms (first term in both equations) while the movement of the surface of the CV is reflected as additional mass and momentum fluxes (second term in both equations).

This set of equations have an extra unknown which is the velocity of the domain ( $\mathbf{w}$ ). Another conservation law to close the system is the space conservation law (see section 3.3), which guarantees the conservation of space (volume) in the moving domain:

$$\frac{d}{dt} \int_v dv - \int_s \mathbf{w} \cdot d\mathbf{A} = 0 \quad (51)$$

Comparing Eq. (49) and (51) (and assuming incompressibility) we realize that the equation of conservation of mass on the moving domain is identical to that equation in a fixed domain:

$$\int_s \rho \mathbf{u} \cdot d\mathbf{A} = \sum_{pn \in s} \dot{m}_{pn} = 0 \quad (52)$$

where  $\dot{m}_{pn}$  is the mass flux at the face  $pn$  and the summation  $\sum_{pn \in s}$  is over all the faces of the CV. Surface integrals at the faces are approximated using the mid-point rule, evaluating the mass flux at a given face as  $\dot{m}_{pn} = \rho_{pn} \mathbf{u}_{pn} \cdot \mathbf{A}_{pn}$ , where the density and velocity are evaluated at the centroid of the face (here, the density is constant as we consider incompressible flow).

The momentum equation is solved using a projection method as described in section 3.1 (Eq. (12)–(16)). The ALE convection-diffusion equation for the predicted velocity field is discretized in time using the second-order method in Eq. (12). In the finite volume method used in this work, the volume integrals are evaluated at their own associated time levels:

$$\begin{aligned} & \frac{1}{\Delta t} \left( \int_{v^{n+1}} \rho \mathbf{u}^* dv - \int_{v^n} \rho \mathbf{u}^n dv \right) = \\ & - \left[ \frac{3}{2} \int_{s^n} \rho \mathbf{u}^n (\mathbf{u}^n - \mathbf{w}^n) \cdot d\mathbf{A} - \frac{1}{2} \int_{s^{n-1}} \rho \mathbf{u}^{n-1} (\mathbf{u}^{n-1} - \mathbf{w}^{n-1}) \cdot d\mathbf{A} \right] \quad (53) \\ & + \frac{\mu}{2} \left( \int_{s^{n+1}} \nabla \mathbf{u}^* \cdot d\mathbf{A} + \int_{s^n} \nabla \mathbf{u}^n \cdot d\mathbf{A} \right) - \int_{s^{n-1/2}} p^{n-1/2} d\mathbf{A} \end{aligned}$$

which is a consistent second-order discretization of the ALE convective-diffusive equation on a moving mesh. The intermediate mesh  $s^{n-1/2}$  for the pressure term is obtained as an average between  $s^n$  and  $s^{n-1}$ :

$$\int_{s^{n-1/2}} p^{n-1/2} d\mathbf{A} = \sum_{pn \in s} p_{pn}^{n-1/2} \mathbf{A}_{pn}^{n-1/2} = \sum_{pn \in s} \frac{1}{2} p_{pn}^{n-1/2} (\mathbf{A}_{pn}^n + \mathbf{A}_{pn}^{n-1}) \quad (54)$$

The convective term is evaluated as some of the fluxes on the faces:

$$\int_s \rho \mathbf{u}(\mathbf{u} - \mathbf{w}) \cdot d\mathbf{A} = \sum_{pn \in s} (\dot{m}_{pn} - \dot{m}_{mesh_{pn}}) \mathbf{u}_{pn} \quad (55)$$

where  $\dot{m}_{mesh_{pn}}$  refers to the additional mass flux due to the movement of the face:

$$\dot{m}_{mesh_{pn}} = \rho_{pn} \mathbf{w}_{pn} \cdot \mathbf{A}_{pn} \quad (56)$$

which will be evaluated using the space conservation law. The velocity on the face centroid to evaluate the mass flux is obtained using a distance-weighted average between the velocities at the grid nodes on either side of the face:

$$\dot{m}_{pn} = \rho \frac{\mathbf{u}_N \delta x_P + \mathbf{u}_P \delta x_N}{\delta x_P + \delta x_N} \cdot \mathbf{A}_{pn} \quad (57)$$

where  $\delta x_P$  and  $\delta x_N$  are the distance between the face centroid and the grid nodes  $P$  and  $N$ , respectively. The convected velocity on the face is evaluated using a symmetry-preserving scheme which is a non-weighted central scheme

$$\mathbf{u}_{pn} = \frac{\mathbf{u}_P + \mathbf{u}_N}{2} \quad (58)$$

as in [49, 50]. The diffusive term is also evaluated on the faces as:

$$\int_s \nabla \mathbf{u} \cdot d\mathbf{A} = \sum_{pn \in s} \nabla \mathbf{u}_{pn} \cdot \mathbf{A}_{pn} \quad (59)$$

and the gradients are evaluated using the neighbouring grid node values. The approximations in equations (57)–(59) and their relation with the overall discretization are similar to the case of a constant domain problem (Eulerian form) and are described in more details in our previous works [50, 51].

The space conservation law (Eq. (51)) is used to evaluate the additional fluxes due to the mesh velocity in order to be used in the momentum equation (Eq. (50), (53) and (55)). In the discretized form, the change of volume of the CV could be represented by the sum of the volumes swept by the faces of that CV. A first-order discretization of this equation reads:

$$\frac{v^{n+1} - v^n}{\Delta t} = \sum_{pn \in s} \frac{\delta v_{pn}^{n+1}}{\Delta t} \quad (60)$$

which is used, for example, in [17, 20]. In this equation  $\delta v_{pn}^{n+1}$  indicates the volume swept by the face  $pn$  (as in figure 1). Thus, the additional flux in the momentum equation could be approximated as  $\dot{m}_{mesh_{pn}}^{n+1} = \rho \frac{\delta v_{pn}^{n+1}}{\Delta t}$ , which is first-order in time (see e.g. [17, 20]).

Alternatively, a second-order discretization of this equation is used in the current work:

$$\frac{3v^{n+1} - 4v^n + v^{n-1}}{2\Delta t} = \sum_{pn \in s} \frac{3\delta v_{pn}^{n+1} - \delta v_{pn}^n}{2\Delta t} \quad (61)$$

which uses the information of the swept volume by face  $pn$  in the two consecutive time steps to obtain second-order accuracy. Thus, the additional flux in the momentum equation is approximated by

$$\dot{m}_{mesh_{pn}}^{n+1} = \rho \frac{3\delta v_{pn}^{n+1} - \delta v_{pn}^n}{2\Delta t} \quad (62)$$

to be used in Eq. (55).

## 8. References

- [1] Y. Bazilevs, V. M. Calo, Y. Zhang, T. J. R. Hughes, Isogeometric fluid-structure interaction analysis with applications to arterial blood flow, *Computational Mechanics* 38 (4-5) (2006) 310–322. doi:10.1007/s00466-006-0084-3.
- [2] A. Borghi, N. B. Wood, R. H. Mohiaddin, X. Y. Xu, Fluid-solid interaction simulation of flow and stress pattern in thoracoabdominal aneurysms: a patient-specific study, *Journal of Fluids and Structures* 24 (2) (2008) 270–280. doi:10.1016/j.jfluidstructs.2007.08.005.
- [3] D. Shiels, A. Leonard, A. Roshko, Flow-induced vibration of a circular cylinder at limiting structural parameters, *Journal of Fluids and Structures* 15 (1) (2001) 3–21. doi:10.1006/jfls.2000.0330.
- [4] P. Bearman, Circular cylinder wakes and vortex-induced vibrations, *Journal of Fluids and Structures* 27 (5) (2011) 648–658. doi:10.1016/j.jfluidstructs.2011.03.021.

- [5] J. Degroote, Partitioned simulation of fluid-structure interaction, *Archives of Computational Methods in Engineering* 20 (2013) 185–238. doi:10.1007/s11831-013-9085-5.
- [6] G. Hou, J. Wang, A. Layton, Numerical methods for fluid-structure interaction - A review, *Communications in Computational Physics* 12 (2) (2012) 337–377. doi:10.4208/cicp.291210.290411s.
- [7] P. Causin, J. F. Gerbeau, F. Nobile, Added-mass effect in the design of partitioned algorithms for fluid-structure problems, *Computer Methods in Applied Mechanics and Engineering* 194 (2005) 4506–4527. doi:10.1016/j.cma.2004.12.005.
- [8] C. Förster, W. A. Wall, E. Ramm, Artificial added mass instabilities in sequential staggered coupling of nonlinear structures and incompressible viscous flows, *Computer Methods in Applied Mechanics and Engineering* 196 (2007) 1278–1293. doi:10.1016/j.cma.2006.09.002.
- [9] P. Le Tallec, J. Mouro, Fluid structure interaction with large structural displacements, *Computer Methods in Applied Mechanics and Engineering* 190 (24-25) (2001) 3039–3067. doi:10.1016/S0045-7825(00)00381-9.
- [10] J. F. Gerbeau, M. Vidrascu, A quasi-Newton algorithm based on a reduced model for fluid-structure interaction problems in blood flows, *ESAIM: Mathematical Modelling and Numerical Analysis* 37 (2003) 631–647. doi:10.1051/m2an:2003049.
- [11] E. Kuhl, S. Hulshoff, R. De Borst, An arbitrary lagrangian eulerian finite-element approach for fluid-structure interaction phenomena, *International Journal for Numerical Methods in Engineering* 57 (1) (2003) 117–142. doi:10.1002/nme.749.
- [12] F. Nobile, C. Vergara, An effective fluid-structure interaction formulation for vascular dynamics by generalized robin conditions, *SIAM Journal on Scientific Computing* 30 (2) (2008) 731–763. doi:10.1137/060678439.
- [13] S. Badia, F. Nobile, C. Vergara, Fluid-structure partitioned procedures based on Robin transmission conditions, *Journal of Computational Physics* 227 (14) (2008) 7027–7051. doi:10.1016/j.jcp.2008.04.006.

- [14] M. A. Fernández, J. Mullaert, M. Vidrascu, Explicit robin–neumann schemes for the coupling of incompressible fluids with thin-walled structures, *Computer Methods in Applied Mechanics and Engineering* 267 (2013) 566–593. doi:10.1016/j.cma.2013.09.020.
- [15] M. A. Fernández, J.-F. Gerbeau, C. Grandmont, A projection semi-implicit scheme for the coupling of an elastic structure with an incompressible fluid, *International Journal for Numerical Methods in Engineering* 69 (4) (2007) 794–821. doi:10.1002/nme.1792.
- [16] A. J. Chorin, Numerical solution of the Navier-Stokes equations, *Mathematics of Computation* 22 (1968) 745–762. doi:10.2307/2004575.
- [17] M. Breuer, G. De Nayer, M. Münsch, T. Gallinger, R. Wüchner, Fluid-structure interaction using a partitioned semi-implicit predictor-corrector coupling scheme for the application of large-eddy simulation, *Journal of Fluids and Structures* 29 (2012) 107–130. doi:10.1016/j.jfluidstructs.2011.09.003.
- [18] M. Astorino, F. Chouly, M. A. Fernández, Robin based semi-implicit coupling in fluid-structure interaction: Stability analysis and numerics, *SIAM Journal on Scientific Computing* 31 (6) (2009) 4041–4065. doi:10.1137/090749694.
- [19] A. Naseri, O. Lehmkuhl, I. Gonzalez, A. Oliva, Partitioned semi-implicit methods for simulation of biomechanical fluid-structure interaction problems, *Journal of Physics: Conference Series* 745 (3) (2016) 032020. doi:10.1088/1742-6596/745/3/032020.
- [20] A. Naseri, O. Lehmkuhl, I. Gonzalez, E. Bartrons, C. D. Pérez-Segarra, A. Oliva, A semi-implicit coupling technique for fluid–structure interaction problems with strong added-mass effect, *Journal of Fluids and Structures* 80 (2018) 94–112. doi:10.1016/j.jfluidstructs.2018.03.012.
- [21] I. González, O. Lehmkuhl, A. Naseri, J. Rigola, A. Oliva, Fluid-structure interaction of a reed type valve, in: *International Compressor Engineering Conference*, Purdue University Libraries, 2016, p. 2490.
- [22] I. González, A. Naseri, J. Rigola, C. D. Pérez-Segarra, A. Oliva, A fluid-structure interaction solver for the fluid flow through reed type valves,

- IOP Conference Series: Materials Science and Engineering 232 (1) (2017) 012032. doi:10.1088/1757-899X/232/1/012032.
- [23] A. Amani, A. Naseri, C. D. Perez-Segarra, A. Oliva, A method for fluid-structure interaction problems with non-newtonian fluid, in: 6th European Conference on Computational Mechanics (ECCM-ECFD 2018), ECCOMAS, Glasgow, UK, June 2018.
- [24] T. He, A cbs-based partitioned semi-implicit coupling algorithm for fluid-structure interaction using mcibc method, *Computer Methods in Applied Mechanics and Engineering* 298 (2016) 252–278. doi:doi.org/10.1016/j.cma.2015.09.020.
- [25] T. He, K. Zhang, T. Wang, Ac-cbs-based partitioned semi-implicit coupling algorithm for fluid-structure interaction using stabilized second-order pressure scheme, *Communications in Computational Physics* 21 (5) (2017) 1449–1474. doi:10.4208/cicp.OA-2016-0106.
- [26] S. Sy, C. M. Murea, A stable time advancing scheme for solving fluid-structure interaction problem at small structural displacements, *Computer Methods in Applied Mechanics and Engineering* 198 (2) (2008) 210–222. doi:10.1016/j.cma.2008.07.010.
- [27] F. Nobile, M. Pozzoli, C. Vergara, Time accurate partitioned algorithms for the solution of fluid-structure interaction problems in haemodynamics, *Computers & Fluids* 86 (2013) 470–482. doi:10.1016/j.compfluid.2013.07.031.
- [28] J. Liu, R. K. Jaiman, P. S. Gurugubelli, A stable second-order scheme for fluidstructure interaction with strong added-mass effects, *Journal of Computational Physics* 270 (2014) 687–710. doi:10.1016/j.jcp.2014.04.020.
- [29] D. L. Brown, R. Cortez, M. L. Minion, Accurate projection methods for the incompressible navier-stokes equations, *Journal of Computational Physics* 168 (2) (2001) 464–499. doi:10.1006/jcph.2001.6715.
- [30] S. Armfield, R. Street, An analysis and comparison of the time accuracy of fractional-step methods for the navier-stokes equations on staggered grids, *International Journal for Numerical Methods in Fluids* 38 (3) (2002) 255–282. doi:10.1002/fd.217.

- [31] J. L. Guermond, P. Mineev, J. Shen, An overview of projection methods for incompressible flows, *Computer Methods in Applied Mechanics and Engineering* 195 (44-47) (2006) 6011–6045. doi:10.1016/j.cma.2005.10.010.
- [32] P. Geuzaine, C. Grandmont, C. Farhat, Design and analysis of ALE schemes with provable second-order time-accuracy for inviscid and viscous flow simulations, *Journal of Computational Physics* 191 (1) (2003) 206–227. doi:10.1016/S0021-9991(03)00311-5.
- [33] C. Farhat, K. G. van der Zee, P. Geuzaine, Provably second-order time-accurate loosely-coupled solution algorithms for transient nonlinear computational aeroelasticity, *Computer Methods in Applied Mechanics and Engineering* 195 (2006) 1973–2001. doi:10.1016/j.cma.2004.11.031.
- [34] O. Oyekole, C. Trenchea, M. Bukac, A second-order in time approximation of fluid-structure interaction problem, *SIAM Journal on Numerical Analysis* 56 (1) (2018) 590–613. doi:10.1137/17M1140054.
- [35] J. Van Kan, A second-order accurate pressure-correction scheme for viscous incompressible flow, *SIAM Journal on Scientific and Statistical Computing* 7 (3) (1986) 870–891. doi:10.1137/0907059.
- [36] J. B. Bell, P. Colella, H. M. Glaz, A second-order projection method for the incompressible navier-stokes equations, *Journal of Computational Physics* 85 (2) (1989) 257–283. doi:10.1016/0021-9991(89)90151-4.
- [37] R. Verzicco, P. Orlandi, A finite-difference scheme for three-dimensional incompressible flows in cylindrical coordinates, *Journal of Computational Physics* 123 (2) (1996) 402–414. doi:10.1006/jcph.1996.0033.
- [38] J. Kim, P. Moin, Application of a fractional-step method to incompressible navier-stokes equations, *Journal of Computational Physics* 59 (2) (1985) 308–323. doi:10.1016/0021-9991(85)90148-2.
- [39] O. Estruch, O. Lehmkuhl, R. Borrell, C. D. P. Segarra, A. Oliva, A parallel radial basis function interpolation method for unstructured dynamic meshes, *Computers and Fluids* 80 (2013) 44–54. doi:10.1016/j.compfluid.2012.06.015.

- [40] H. Wendland, Piecewise polynomial, positive definite and compactly supported radial functions of minimal degree, *Advances in Computational Mathematics* 4 (1) (1995) 389–396. doi:10.1007/BF02123482.
- [41] U. Küttler, W. A. Wall, Fixed-point fluid-structure interaction solvers with dynamic relaxation, *Computational Mechanics* 43 (2008) 61–72. doi:10.1007/s00466-008-0255-5.
- [42] L. Formaggia, J. F. Gerbeau, F. Nobile, A. Quarteroni, On the coupling of 3D and 1D Navier-Stokes equations for flow problems in compliant vessels, *Computer Methods in Applied Mechanics and Engineering* 191 (6-7) (2001) 561–582. doi:10.1016/S0045-7825(01)00302-4.
- [43] M. A. Fernández, M. Landajuela, M. Vidrascu, Fully decoupled time-marching schemes for incompressible fluid/thin-walled structure interaction, *Journal of Computational Physics* 297 (2015) 156–181. doi:10.1016/j.jcp.2015.05.009.
- [44] L. Li, W. D. Henshaw, J. W. Banks, D. W. Schwendeman, A. Main, A stable partitioned FSI algorithm for incompressible flow and deforming beams, *Journal of Computational Physics* 312 (2016) 272–306. doi:10.1016/j.jcp.2016.02.002.
- [45] A. Quarteroni, M. Tuveri, A. Veneziani, Computational vascular fluid dynamics: Problems, models and methods, *Computing and Visualization in Science* 2 (2000) 163–197. doi:10.1007/s007910050039.
- [46] P. Anagnostopoulos, P. Bearman, Response characteristics of a vortex-excited cylinder at low reynolds numbers, *Journal of Fluids and Structures* 6 (1) (1992) 39–50. doi:10.1016/0889-9746(92)90054-7.
- [47] K. W. Schulz, Y. Kallinderis, Unsteady flow structure interaction for incompressible flows using deformable hybrid grids, *Journal of Computational Physics* 143 (2) (1998) 569–597. doi:10.1006/jcph.1998.5969.
- [48] J. Yang, S. Preidikman, E. Balaras, A strongly coupled, embedded-boundary method for fluid–structure interactions of elastically mounted rigid bodies, *Journal of Fluids and Structures* 24 (2) (2008) 167–182. doi:10.1016/j.jfluidstructs.2007.08.002.

- [49] R. Verstappen, A. Veldman, Symmetry-preserving discretization of turbulent flow, *Journal of Computational Physics* 187 (1) (2003) 343–368. doi:10.1016/S0021-9991(03)00126-8.
- [50] F. X. Trias, O. Lehmkuhl, A. Oliva, C. D. Pérez-Segarra, R. W. C. P. Verstappen, Symmetry-preserving discretization of Navier-Stokes equations on collocated unstructured grids, *Journal of Computational Physics* 258 (2014) 246–267. doi:10.1016/j.jcp.2013.10.031.
- [51] L. Jofre, O. Lehmkuhl, J. Ventosa, F. X. Trias, A. Oliva, Conservation properties of unstructured finite-volume mesh schemes for the navier-stokes equations, *Numerical Heat Transfer, Part B: Fundamentals* 65 (1) (2014) 53–79. doi:10.1080/10407790.2013.836335.